



**Manchester  
Metropolitan  
University**

---

Higginbottom, T and Symeonakis, Ilias and Meyer, H and van der Linden, S (2018) *Mapping fractional woody cover in semi-arid savannahs using multi-seasonal composites from Landsat data*. ISPRS Journal of Photogrammetry and Remote Sensing, 139. pp. 88-102. ISSN 0924-2716 (In Press)

---

**Downloaded from:** <http://e-space.mmu.ac.uk/619555/>

**Version:** Accepted Version

**Publisher:** Elsevier

**DOI:** <https://doi.org/10.1016/j.isprsjprs.2018.02.010>

**Usage rights:** Creative Commons: Attribution-Noncommercial-No Derivative Works 4.0

Please cite the published version

<https://e-space.mmu.ac.uk>

# Mapping Woody Cover in Semi-arid Savannahs using Multi-seasonal Composites from Landsat Data

Thomas P Higginbottom <sup>a\*</sup>, Elias Symeonakis<sup>a</sup>, Hanna Meyer<sup>b</sup> and Sebastian van der Linden<sup>c</sup>

<sup>a</sup> School of Science and the Environment, John Dalton Building, Manchester Metropolitan University, Manchester, M1 5GD, United Kingdom

<sup>b</sup> Environmental Informatics, Faculty of Geography, Philipps- Universität Marburg, Marburg, Germany

<sup>c</sup> Geography Department, Humboldt-Universität zu Berlin, Berlin, Germany

\*Corresponding Author: [T.Higginbottom@mmu.ac.uk](mailto:T.Higginbottom@mmu.ac.uk), Room 418 John Dalton East.

## Abstract

Increasing attention is being directed at mapping the fractional woody cover of savannahs using Earth-observation data. In this study, we test the utility of Landsat TM/ ETM-based spectral-temporal variability metrics for mapping regional-scale woody cover in the Limpopo Province of South Africa, for 2010. We employ a machine learning framework to compare the accuracies of Random Forest models derived using metrics calculated from different seasons. We compare these results to those from fused Landsat-PALSAR data to establish if seasonal metrics can compensate for structural information from the PALSAR signal. Furthermore, we test the applicability of a statistical variable selection method, the recursive feature elimination (RFE), in the automation of the model building process in order to reduce model complexity and processing time. All of our tests were repeated at four scales (30, 60, 90, and 120 m-pixels) to investigate the role of spatial resolution on modelled accuracies.

Our results show that multi-seasonal composites combining imagery from both the dry and wet seasons produced the highest accuracies ( $R^2= 0.77$ , RMSE=9.4, at the 120 m scale). When using a single season of observations, dry season imagery performed best ( $R^2=0.74$ , RMSE=9.9, at the 120 m

27 resolution). Combining Landsat and radar imagery was only marginally beneficial, offering a mean  
28 relative improvement of 1% in accuracy at the 120 m scale. However, this improvement was  
29 concentrated in areas with lower densities of woody coverage (<30%), which are areas of concern for  
30 environmental monitoring. At finer spatial resolutions, the inclusion of SAR data actually reduced  
31 accuracies. Overall, the RFE was able to produce the most accurate model ( $R^2=0.8$ ,  $RMSE=8.9$ , at the  
32 120 m pixel scale). For mapping savannah woody cover at the 30 m pixel scale, we suggest that  
33 monitoring methodologies continue to exploit the Landsat archive, but should aim to use multi-  
34 seasonal derived information. When the coarser 120 m pixel scale is adequate, integration of Landsat  
35 and SAR data should be considered, especially in areas with lower woody cover densities. The use of  
36 multiple seasonal compositing periods offers promise for large-area mapping of savannahs, even in  
37 regions with a limited historical Landsat coverage.

38

39 Keywords:

- 40 • Landsat-metrics;
- 41 • Optical-radar fusion;
- 42 • woody cover mapping;
- 43 • Savannahs;
- 44 • Large-area mapping

45

## 46 1 Introduction

47 Savannah ecosystems are characterised by a dynamic mosaic of tree, shrub and grass species.  
48 Variations in these components can result in widely divergent ecological functions (Sankaran et al.,  
49 2005). There is growing concern over the health and sustainability of savannahs across the world.  
50 Increases in shrub cover at the expense of grasslands (i.e. shrub encroachment) have been reported  
51 in semi-arid environments globally (Naito and Cairns 2011, Stevens et al., 2016, Tian et al., 2016,  
52 Skowno et al., 2017). In contrast, overexploitation of woody shrubs and trees for fuelwood may be  
53 depleting woody cover in other regions (Wessels et al., 2013, Brandt et al., 2017).

54 Monitoring savannahs is a challenging endeavour, and due to the discontinuous nature of land  
55 cover in such environments, categorical maps are of limited value. Alternatively, representing the 2-  
56 dimension horizontal woody cover component as a continuous fractional layer is more ecologically  
57 relevant, and recent advances in the field have focused their attention to this characteristic (Bucini et  
58 al., 2010, Armston 2009, Naidoo et al., 2016). However, the spatial heterogeneity of savannahs makes  
59 fractional cover modelling vulnerable to scale effects, as areas of very high or low coverage will be lost  
60 by aggregation to coarser scales (Guerschman et al., 2009). Therefore, it is necessary to consider  
61 analyses over a range of resolutions, enabling an optimum balance between model accuracy and  
62 spatial detail to be established (Urbazaev et al., 2015).

63 Passive optical Earth observation (EO) data, such as Landsat, have commonly been employed to  
64 map savannah vegetation in the past (Prince and Astle 1986). Such data discriminate vegetation type  
65 by exploiting the full spectral range of reflected solar radiation. Passive optical data also allow for  
66 vegetation indices, such as the Normalized Difference Vegetation Index (NDVI), to be used as proxies  
67 of various biogeophysical parameters, such as net primary productivity (NPP), fraction of  
68 photosynthetically active radiation (fPAR), and leaf area index (LAI) (Carlson and Ripley 1997,  
69 Higginbottom and Symeonakis 2014, Zhu et al., 2013). Yet single date optical imagery can be  
70 inappropriate for discriminating woody and grass coverage, as photosynthetic activity is detected  
71 indiscriminately (Olsson, Leeuwen, and Marsh 2011). In savannahs, the woody cover component  
72 decreases temporal variation within the NDVI signal, as bushes and shrubs maintain leaves  
73 throughout the dry season (Bucini et al., 2010, Naidoo et al., 2016). Information derived from a pixel-  
74 level time series can therefore contain valuable information for land cover mapping. If sufficient  
75 observations are available, phenological metrics detailing the start and end points of seasons can be  
76 calculated (Brandt et al., 2016). Alternatively, spectral-temporal variability metrics from single  
77 spectral bands or indices (e.g. minimum, maximum, mean, median, etc.) can quantify variability even  
78 in regions with lower observation densities (Müller et al., 2015, Zhong, Gong, and Biging 2014).

79 Irrespective of processing method, optical data possesses fundamental limitations for mapping  
80 woody environments, because it does not directly correlate to surface structure (Naidoo et al., 2016).  
81 Active EO sensors such as Synthetic Aperture Radar (SAR) provide information on the 3-dimensional  
82 structure of the land surface, by emitting microwaves and measuring the intensity of energy reflected  
83 back to the sensor after interactions with ground objects i.e. the *backscatter* ( $\sigma^0$ ) of the signal. The  
84 use of SAR data in fractional woody cover mapping, particularly L-band, operating with wavelengths  
85 of 0-15 cm , has been well demonstrated (Bucini et al., 2010, Mathieu et al., 2013, Naidoo et al., 2015,  
86 2016). Mitchard et al., (2009) identified a consistent relationship between cross-polarised L-band  
87 backscatter and aboveground biomass (AGB) across four pan-African tropical savannahs, regardless  
88 of vegetation composition. Advanced Land Observing Satellite (ALOS) Phased Array type L-band  
89 Synthetic Aperture Radar (PALSAR) imagery has been highlighted as the most reliable satellite-based  
90 indicator of both AGB and canopy coverage for woody cover in semi-arid savannahs (Naidoo et al.,  
91 2015, 2016). However, the use of L-band imagery for mapping long-term land cover change is affected  
92 by a number of data continuity issues, sensor failures (JERS-1, ALOS PALSAR), high data costs, and the  
93 short lifespan of radar systems, resulting in a limited temporal archive compared to Landsat. There  
94 are less limitations when using C-band radar, such as Radarsat or Sentinel-1, due to more consistent  
95 coverage (Reiche et al., 2016 ). However, C-band radar is not as sensitive to woody cover, compared  
96 to L-band (Mathieu et al., 2013).

97 More recently, the fusion of optical and radar imagery has been shown to provide an  
98 improvement upon single-sensor fractional cover accuracies (Bucini et al., 2010, Naidoo et al., 2016).  
99 Bucini et al., (2010) and Naidoo et al., (2016) combined L-band radar data with Landsat to map woody  
100 canopy coverage in the Kruger National Park, South Africa: the fusion approach improved the accuracy  
101 over single sensor predictions, particularly when combining SAR with multi-season imagery. Lucas et  
102 al., (2006) used PALSAR thresholds in conjunction with Landsat-derived Foliage Projected Cover maps  
103 to successfully discriminate regrowth stages in open Eucalyptus forests. Merging various SAR  
104 wavebands, such as C, X, or L, have also been shown to provide benefits for woody cover mapping,

105 although these improvements were found to be smaller (~3%) when compared with L-band alone  
106 (Naidoo et al., 2015). Choosing the appropriate sensor, or combination of sensors, for woody cover  
107 mapping, is therefore an increasingly complex decision with further study required.

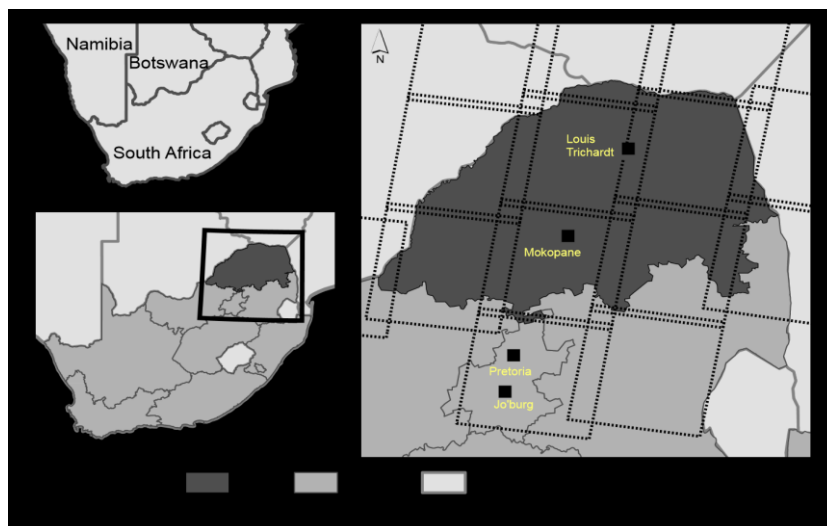
108 The increasing number and variety of EO systems in operation, coupled with open-data policies,  
109 presents a wide range of pathways for land cover mapping. Compared to earlier investigations, it is  
110 now routine for studies to use high-dimensional data. However, this approach comes with statistical  
111 limitations. Predictive models trained using high-dimensional data are prone to overfitting, thus  
112 transferring poorly to unseen validation data. This issue is important, potentially incurring a high  
113 degree of variance into classifications, whilst reducing bias (i.e. the bias-variance dilemma) (James et  
114 al., 2013, Kuhn and Johnson 2013). A number of techniques exist to process high-dimensional data  
115 and extract the most relevant variables, aiming to reduce model complexity whilst retaining predictive  
116 accuracy (Guyon et al., 2002, Guyon and Elisseeff 2003). To date the implementation of these methods  
117 in remote sensing analyses has been limited (Meyer et al., 2016), but may be increasingly beneficial in  
118 the near future as the number of data sources continues to increase.

119 Within this context, the overarching aim of this study is to develop a framework for accurately  
120 mapping the fractional woody cover of semi-arid savannahs at large spatial scales, using freely and  
121 widely available data sources. We address this overarching aim by carrying out a multi-scale  
122 comparative exercise that provides answers to the following questions:

- 123 1. Can annual time series of Landsat metrics be used to accurately map fractional woody cover,  
124 and to what extent does seasonality of the compositing period influence results?
- 125 2. How do Landsat-based estimates compare to multi-sensor fusion approaches combining L-  
126 band SAR data?
- 127 3. Can automated variable selection methods, such as Recursive Feature Elimination, assist in  
128 reducing the number of variables used without compromising accuracy?

129 **2 Study Area**

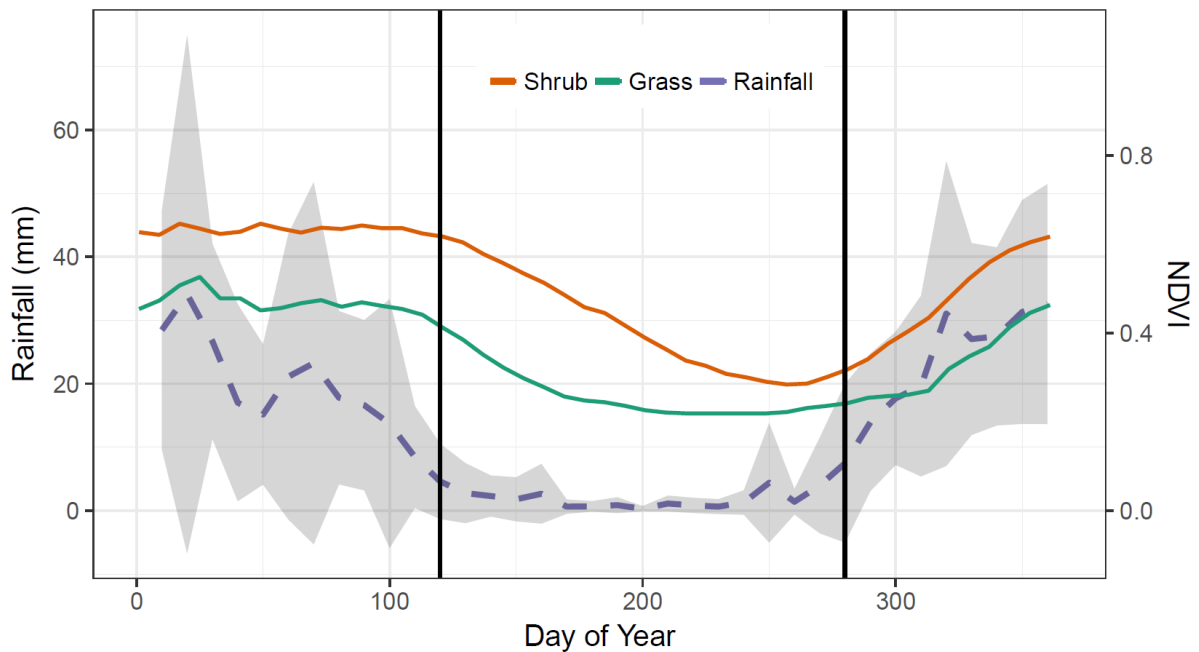
130 Our study area is the Limpopo Province, South Africa (Fig 1). The province is ~125,000 km<sup>2</sup> and  
131 intersects 14 Landsat WRS-2 scenes. This region is predominantly open deciduous savannah and  
132 grassland, with discontinuous woody cover ranging from 0-60% coverage (Mucina and Rutherford  
133 2006). The climate is mainly semi-arid with small humid subtropical areas (Kottek et al., 2006). Mean  
134 annual temperatures range from 21-23°C and winters are mild and frost-free (Scholes et al., 2001).  
135 Rainfall increases along a north-south gradient, with mean annual precipitation of 450 mm/year in  
136 the north, rising to 700 mm/year in the south (Scholes et al., 2001). The majority of rainfall occurs in  
137 the winter months (October to March; Fig 2).



138

139 Figure 1: Location of the study area, the Limpopo Province of South Africa

140



141

142 Figure 2: Annual seasonality of NDVI for a dense shrub and grassland pixel, and regional rainfall for  
143 the Limpopo Province. NDVI is the mean value from 15 year of MODIS-MCD43A4 16 day  
144 observations, rainfall data is the mean and standard deviations from FEWS-NET  
145 (<https://www.fews.net/>). The vertical lines indicate the start and the end of the dry season.

146 There are pronounced contrasts in land use intensity across the region. In the east, the  
147 Kruger National Park is the largest protected area in South Africa featuring minimal human usage  
148 beyond fire experiments and animal enclosures. This contrasts with the communally governed areas  
149 originating from apartheid-era homelands (Worden 2012). These areas generally feature very high  
150 population densities ranging from 200-300 people per km<sup>2</sup>, resulting from forced resettlement in  
151 the 1960-1990 apartheid period (Pollard et al., 2003). Consequently, overgrazing and unsustainable  
152 wood harvesting are widespread with many areas classified as degraded (Wessels et al., 2013).



## 153 3 Data

### 154 3.1 Training and validation data

155 We aimed to develop a transferable method for woody cover mapping. Accordingly, we used  
156 training and validation data from aerial imagery, so that our methodological framework would be  
157 applicable in study areas where such imagery is available but other data may not be or are costly, e.g.  
158 field surveys, Lidar. In South Africa, the National Geospatial Information (NGI) agency of the  
159 Department of Rural Development and Land Reform have been providing 0.5 m colour aerial  
160 photography since 2008 , with an orthorectification accuracy of  $\pm 3$  m (NGI 2017) . Six 5×5 km images  
161 were selected according to a stratified approach based on mean annual precipitation, with acquisition  
162 dates between the 19<sup>th</sup> April and 7<sup>th</sup> August of the years 2008 and 2009 (Appendix 1).

### 163 3.2 Satellite imagery

#### 164 3.2.1 Landsat

165 Spectral-temporal variability metrics are a method of capturing information on the temporal  
166 evolution of spectral values within a pixel (Muller et al., 2016). We hypothesised that metrics  
167 capturing this variability would be effective for woody cover monitoring. To generate metrics, all  
168 available Landsat 5 and 7 images that intersected the Limpopo Province for 2009-2010 were used, for  
169 the wet season additional images from the two neighbouring hydrological years were also used  
170 (scene footprints shown in Fig 1). Top-of-atmosphere (TOA) reflectance was calculated using standard  
171 bias-gain equations. Pixels affected by clouds or cloud shadow were removed based on the F-mask  
172 algorithm (Zhu and Woodcock 2012), no correction was applied for missing Scan Line Corrector (SLC-  
173 off) pixels. For each pixel, all co-located observations were used to calculate the following statistics:  
174 mean, median, minimum, maximum, and standard deviation. These metrics were calculated over  
175 three time-periods: annual, dry season and wet season (Fig 2), resulting in a total of 90 Landsat-

176 derived layers. The number of images used within each observation period is given in Table 1. Due to  
 177 persistent high cloud cover, wet season metrics were calculated over three southern hemisphere  
 178 hydrological years. Processing was undertaken in the Google Earth Engine cloud computing  
 179 environment (Gorelick et al., 2017, Moore and Hansen, 2011).

180

Period	Start Date	End Date	Landsat 5 Images	Landsat 7 Images	Total Images
Annual Cycle	1st January	31st December	86	259	345
Dry Season	1st November	30th April	52	186	238
Wet Season	1st May	1st October	27	102	129
Total Unique Images			88	324	412

181 Table 1: Number of Landsat images used in each period for variability metric calculations. Wet  
 182 season metrics are calculated over three hydrological years: 2009-2010, 2010-2011, and 2011-2012.  
 183 *Total Unique* does not equal the sum of rows as images can be included in both a single season and  
 184 the annual period.

185

### 186 3.2.2 ALOS-PALSAR

187 ALOS PALSAR, and its successor ALOS-2 PALSAR-2, are fully polarimetric L-band Synthetic Aperture  
 188 Radar systems (Rosenqvist et al., 2007). These sensors operate at a wavelength of 23.6 cm. We used  
 189 the 2010 data from the ALOS PALSAR global mosaic, a science-ready product generated annually for  
 190 2007 to 2010 (ALOS), and 2015 (ALOS-2). The images for this mosaic were from the dry season, with  
 191 acquisition dates between 1<sup>st</sup> July - 3<sup>rd</sup> October and two images from 2009. Dual polarization HH  
 192 (horizontal-horizontal) and HV (horizontal-vertical) backscatter data were used. Pre-processing of the  
 193 input raw imagery includes orthorectification using the Shuttle Radar Topography Mission (SRTM)

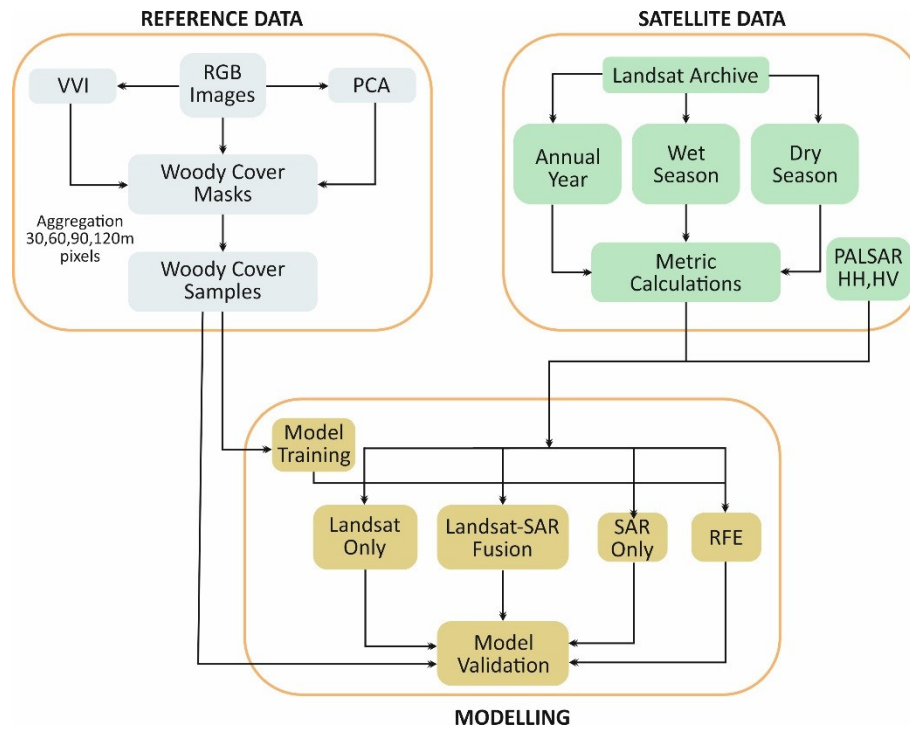
194 Digital Elevation Model (DEM), calibration, speckle reduction, and a destriping procedure (Shimada  
195 and Ohtaki 2010, Shimada et al., 2014). The raw digital number format was converted to backscatter  
196 ( $\sigma^0$ ) using the calibration equation:

$$197 \quad \sigma^0 = 10 * \log_{10}(DN + 0.001)^2 + CF \quad (1)$$

198 where DN is the raw digital number and CF is a calibration factor (= -83). The 25 m mosaic was  
199 resampled to match the Landsat resolution using bilinear resampling.

## 200 4 Methods

201 The methodological framework is shown in Fig 3. To establish the optimum approach for fractional  
202 woody cover mapping, we ran a series of random forest regressions to compare the accuracies  
203 achieved from single season Landsat metrics, multi-season data, or multi-sensor combining Landsat  
204 and SAR data. These models were repeated at four resolutions: 30, 60, 90 and 120 m, to ascertain the  
205 ideal scale for large-area monitoring. Processing was undertaken in the *R* Statistical Software  
206 Environment, using the *raster*, *caret*, and *randomForest* packages (Hijmans et al., 2015, Kuhn 2015,  
207 Liaw and Wiener 2002, *R* Core Team 2015). Fractional cover sampling code was adapted from Leutner  
208 and Horning (2016).



209

210 Figure 3. Flow chart of methodological framework. VVI: Visible Vegetation Index; PCA: Principle  
 211 Components Analysis; RFE: Recursive Feature Elimination.

#### 212 4.1 Creation of Reference Data

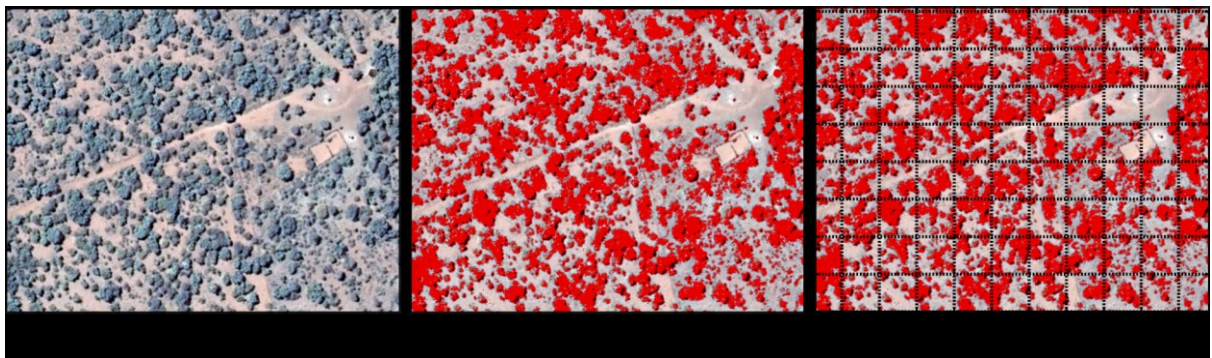
213 To create training data the six aerial imagery subsets were classified into woody/non woody  
 214 masks. We opted for aerial image classification to enable methods to be transferable to other  
 215 locations, due to the generally satisfactory availability of aerial imagery at appropriate scales (Staben  
 216 et al., 2016). Firstly, a principal components analysis (PCA) was applied to the three RGB layers and  
 217 the first two components were extracted. Secondly, we calculated the visible vegetation index  
 218 (Joseph and Devadas 2015) which uses visible light spectra to estimate photosynthetic activity and is  
 219 defined as:

220

$$221 \quad VVI = \left[ \left(1 - \frac{R - R_0}{R + R_0}\right) \left(1 - \frac{G - G_0}{G + G_0}\right) \left(1 - \frac{B - B_0}{B + B_0}\right) \right] \quad (2)$$

222 where VVI is the visible vegetation index,  $R$ ,  $G$  and  $B$  are the red, green, and blue intensities in the  
223 image,  $R_0$ ,  $G_0$  and  $B_0$  are values of red, green, blue used to reference green colour (30, 50, and 1,  
224 respectively), determined by the image bit rate (Joseph and Devadas 2015).

225 A Random Forest classifier was used to create the binary woody-non woody layers from the  
226 original RGB layers, principle components, and VVI. Individual models were generated for each image  
227 using 400 manually selected points per image (75/25% training-validation split). The mean  
228 classification accuracy was 85%. Full accuracy statistics are given in the Appendix. An example  
229 classified mask is shown in Fig 4.



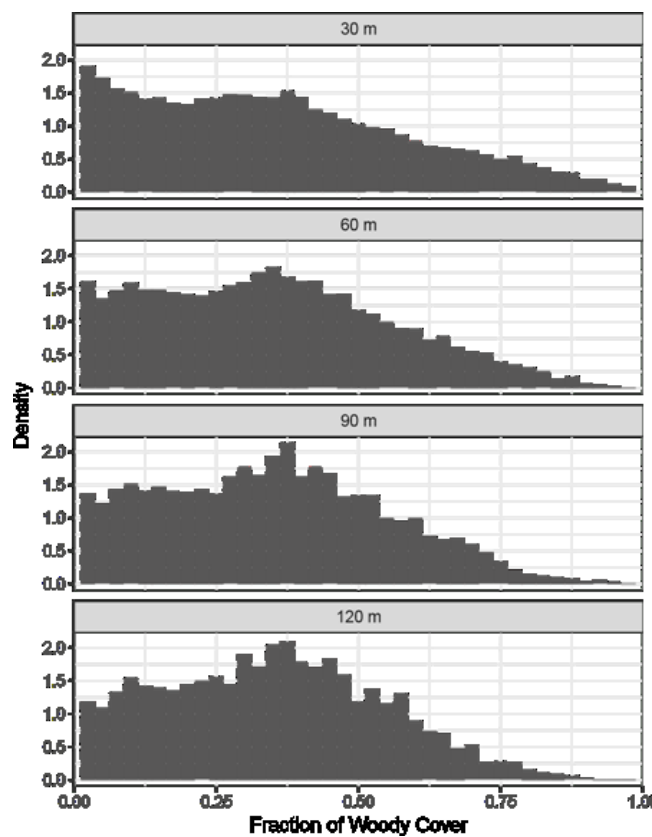
230

231 Figure 4: Example of the RGB woody classification. (a) raw RGB image; (b) classified woody  
232 cover shown in red, and (c) 30 m grid for fractional cover sampling.

233 To generate training and validation data for the satellite imagery, Landsat pixel-sized squares (i.e.  
234 30×30 m) were extracted from the woody/non-woody masks and the percentage woody coverage  
235 calculated. From each image,  $7000/\alpha$  samples were extracted, where  $\alpha$  takes the values of 1, 2, 3 or  
236 4, depending on the aggregation level used to test the effect of scale in the accuracy of the woody  
237 cover estimates (Fig 3). For example, for a pixel size of 30m,  $\alpha=1$  and the samples extracted from each  
238 image are 7000, whereas for an aggregation level of  $\alpha=2$  or a pixel size of 60 m, the number of samples  
239 extracted are  $7000/2=3500$ . These samples were merged and split into equal training and validation  
240 subsets with equal probability distributions of woody cover (Fig 5). The spatial aggregation process  
241 may incur central tendency in training values, with the reduction in high or low samples making the

242 subsequent regression task easier. To quantify this, we tested for any significant difference between  
243 the sample distributions using Pairwise-Wilcoxon tests. These highlighted a significant ( $p < 0.05$ )  
244 difference between the data at 30 m and all other scales which can also be visualised in the relatively  
245 reduced number of high (>75%) and low (<10%) values in the respective aggregated pixel histograms  
246 (Figure 5).

247



248

249 Figure 5: Density histograms of model training values at the four scales tested

## 250 4.2 Random Forest Regression

251 Predictive models were generated using the Random Forest algorithm. Random Forest is an  
252 ensemble machine learning procedure that combines bootstrapping and aggregation (bagging) with  
253 decision trees (Breiman 2001). All models were individually tuned using 10 repeats of 10-fold cross

254 validation to identify the ideal parameter specification. This covered the number of variables  
255 considered at each tree node and the number of trees constructed.

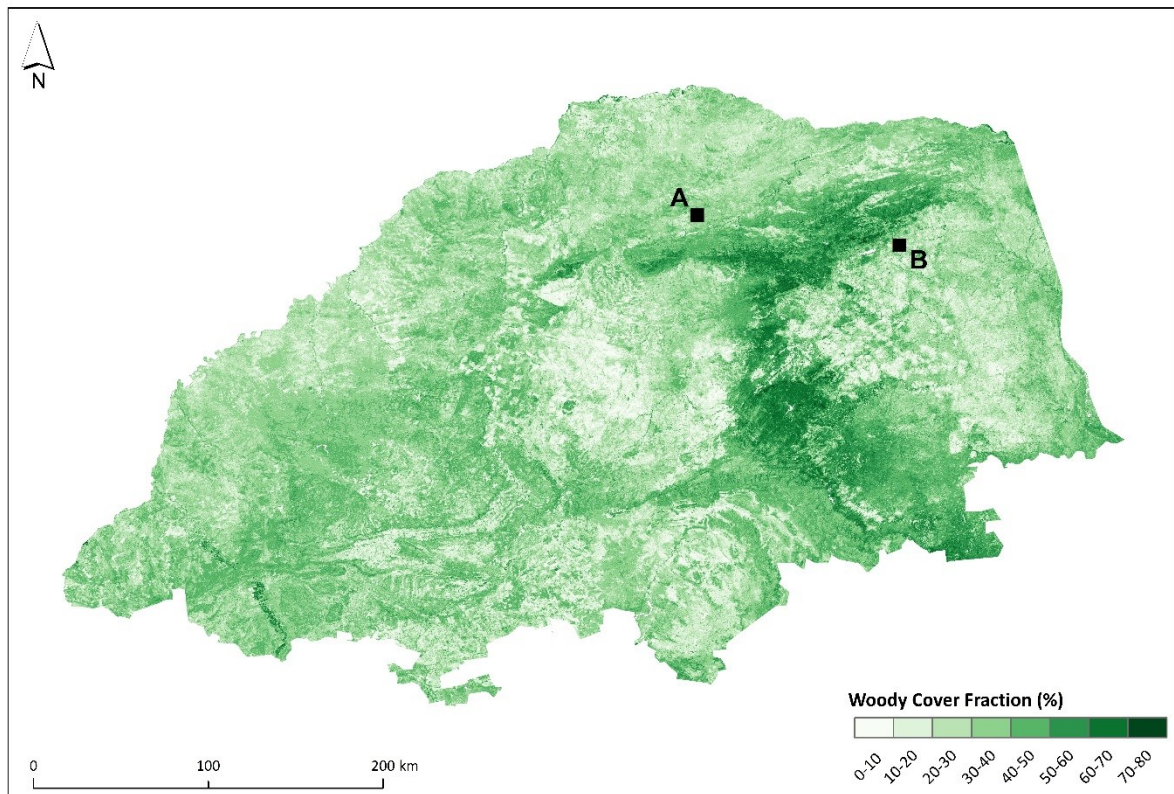
### 256 4.3 Variable Selection

257 To identify optimum predictive models, we incorporated all potential variables into a variable  
258 selection process. According to statistical learning theory, a model containing fewer predictors that  
259 is comparably accurate is preferential to a more complex model (James et al., 2013, Kuhn and Johnson  
260 2013). Backwards selection methods are effective in identifying the ideal number of variables for  
261 prediction, allowing the selection of the most parsimonious model that offers comparable accuracy  
262 (Guyon et al., 2002, James et al., 2013, Kuhn and Johnson 2013). The combination of Landsat metrics  
263 and PALSAR data resulted in 92 predictors (90 Landsat metrics + 2 PALSAR backscatter), a number of  
264 which are correlated. To identify the most important predictors, we implemented the backwards  
265 selection method of recursive feature elimination (RFE). RFE is a parameter selection process that  
266 incorporates the estimation of test (validation) errors and variable importance (Guyon et al., 2002).  
267 Firstly, a model is constructed using all available predictors ( $M_p$ ). The test error of this model (i.e.  
268 adjusted  $R^2$  and RMSE) is then estimated using 10-fold cross validation, and variable importance  
269 scores are calculated. A second model is then established which excludes the lowest contributing  
270 variable from  $M_p$ , and test error and variable importance are recalculated. This process is repeated  
271 until a one-variable model remains. A full iteration of this procedure is repeated 10 times to account  
272 for variations in the cross validation sampling, providing a robust estimate of test errors. An ideal  
273 model that offers the best performance whilst using the least variables can then be selected.

274 **5 Results**

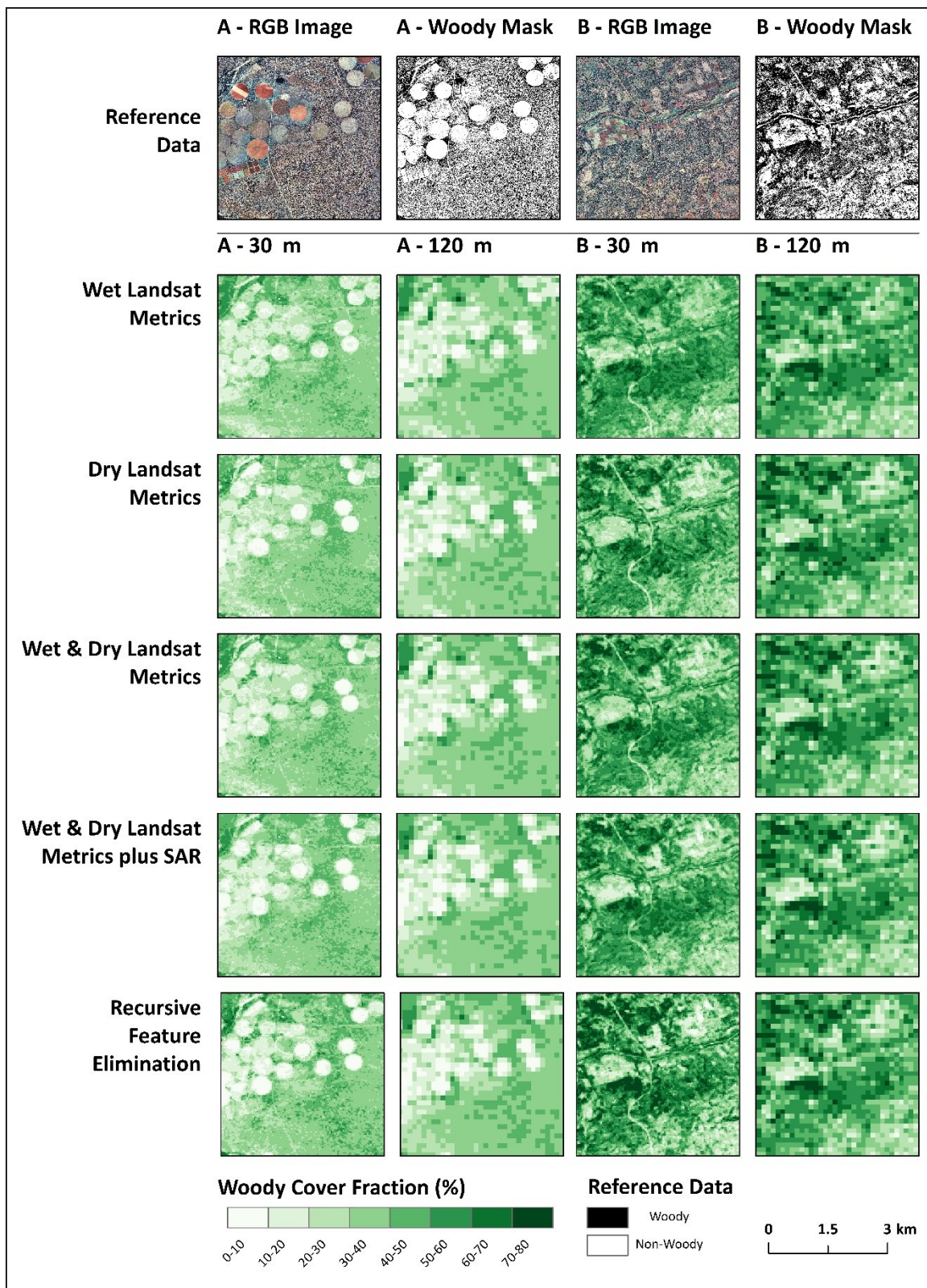
275 **5.1 Woody Cover Mapping**

276 A fractional woody cover map derived from the most accurate model tested, is shown in Fig 6. Subsets  
277 comparing the mapped woody cover estimates from a number of models and the NGI aerial imagery  
278 are shown in Fig 7.



279  
280 Figure 6. Fractional woody cover results for the Limpopo Province based on the Recursive  
281 Feature Elimination model at the 120 m pixel scale. Black squares A and B are the locations of the  
282 subsets in Fig 7.





283

284

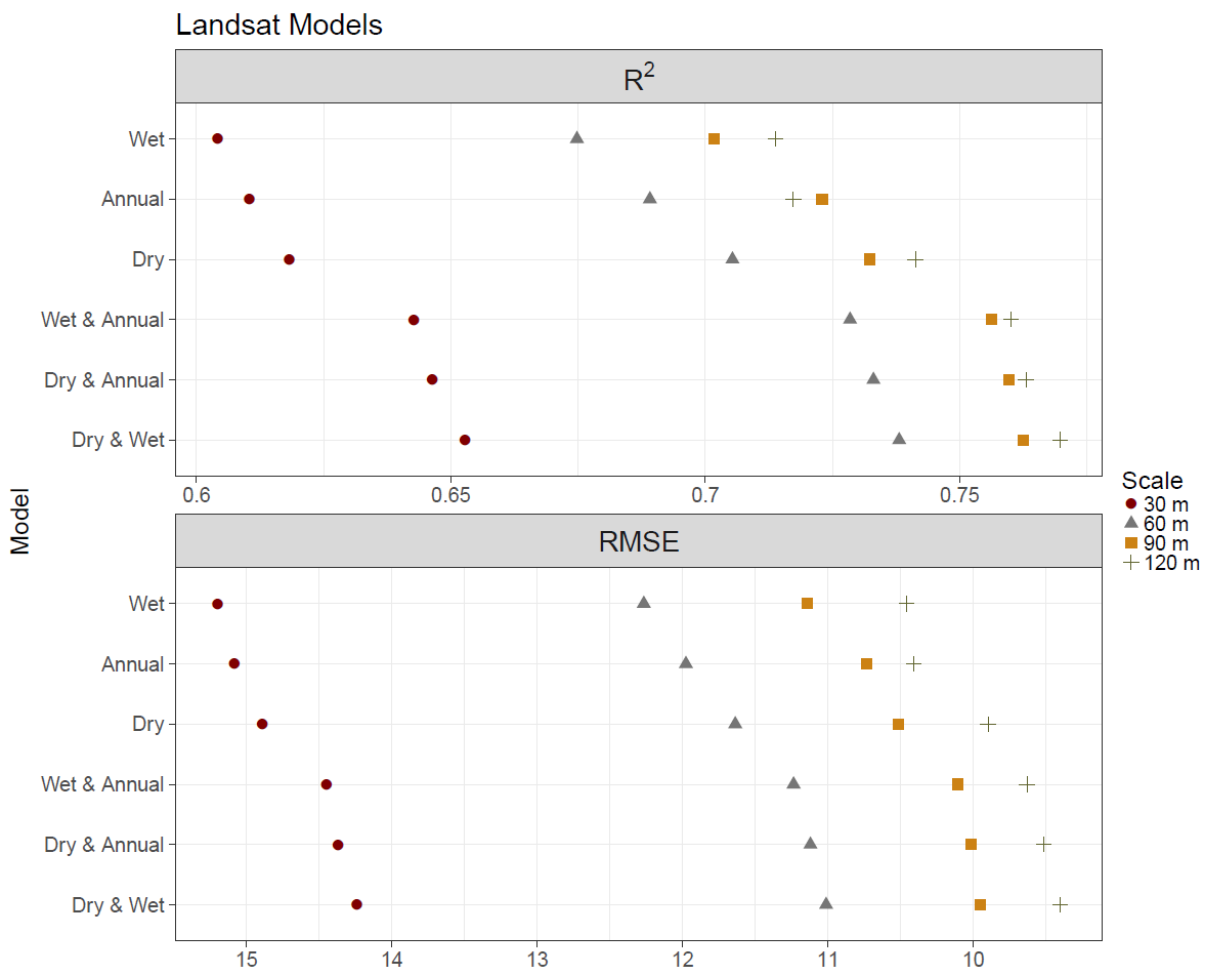
285

286

Figure 7. Spatial patterns of woody cover for subsets A and B of Fig 6 at 30 and 120 m pixel scales. Five model predictions and the respective reference aerial imagery from the NGI are shown. Aerial imagery acquisition dates: A: 19 April 2009, B: 30 April 2009.

287 5.2 Seasonal Landsat models

288 The performance of Landsat-based models is shown in Fig 8 and Table 2. When using metrics  
 289 derived from a single season, the highest accuracies were obtained by using the dry season metrics,  
 290 followed by the full annual cycle, with the wet season performing the worst. This pattern was  
 291 consistent across all scales (Table 2). Using a combination of metrics derived from two seasons, the  
 292 highest accuracies came from models incorporating both dry and wet season data, followed by dry  
 293 and annual, and finally wet and annual (Table 2). Reducing the pixel resolutions (i.e. increasing the  
 294 aggregation factor), consistently raised the model performances, with the largest improvement  
 295 occurring in the initial aggregation from 30 m to 60 m.



296

297 Figure 8. Model accuracy results for Landsat metrics-based models RMSE units are percentage  
 298 woody cover (0-100%)

299

300

301

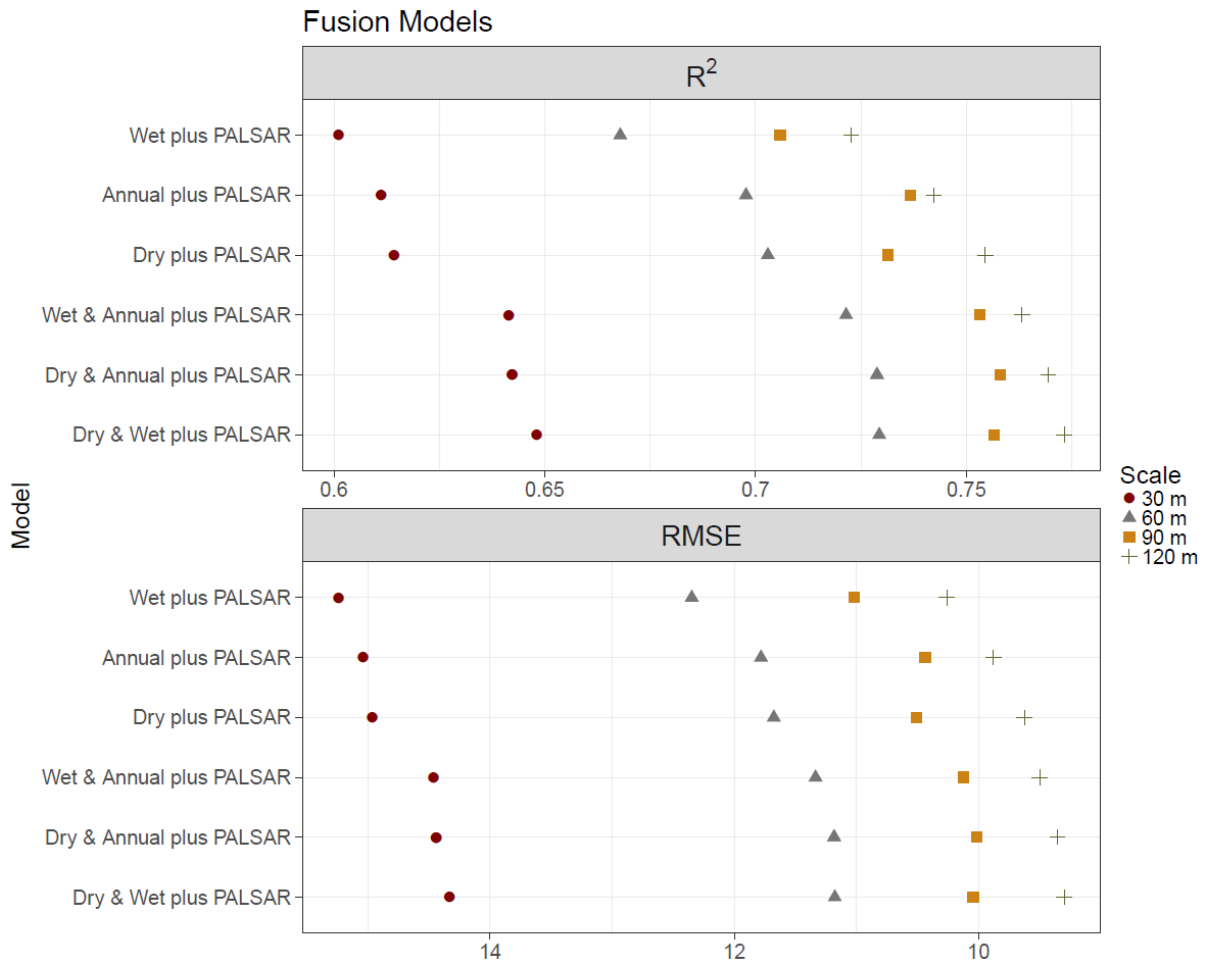
	120 m n-3,848		90 m n-6,826		60 m n-10,499		30 m n-21,000	
	R <sup>2</sup>	RMSE	R <sup>2</sup>	RMSE	R <sup>2</sup>	RMSE	R <sup>2</sup>	RMSE
<b>Landsat Dry and Wet</b>	0.77	9.4	0.762	10	0.738	11	0.653	14.2
<b>Landsat Dry and Annual</b>	0.763	9.5	0.76	10	0.733	11.1	0.646	14.4
<b>Landsat Wet and Annual</b>	0.76	9.6	0.756	10.1	0.728	11.2	0.643	14.4
<b>Landsat Dry</b>	0.741	9.9	0.732	10.5	0.705	11.6	0.618	14.9
<b>Landsat Annual</b>	0.717	10.4	0.723	10.7	0.689	12	0.61	15.1
<b>Landsat Wet</b>	0.714	10.5	0.702	11.1	0.675	12.3	0.604	15.2

302 Table 2. Model accuracy results for the Landsat metrics-based models, RMSE units are percentage  
303 woody cover (0-100%)

### 304 5.3 Fused models

305 Accuracy statistics from models combining Landsat metrics with ALOS PALSAR backscatter are  
306 shown in Fig 9 and Table 3. Overall, the same ranking of seasonal performance as Landsat-only models  
307 was observed. For a single season, accuracy decreased from dry to annual to wet, whilst multi-season  
308 models were ranked: dry and wet, dry and annual, and wet and annual. The only exception to this  
309 order was at the 90 m pixel scale, where the single season annual metrics and dry-annual multi-  
310 season models performed best (Table 4).

311 The fusion of PALSAR backscatter with Landsat metrics had contrasting impacts on model  
312 accuracy (Table 4). At the 120 m scale, all models were improved. Conversely, at the 30 m scale,  
313 performances were negatively affected. At mid-range scales (60 and 90 m), the single season annual  
314 models were improved, as did the 90 m ‘wet’ model. All other mid-scale models responded negatively  
315 to the SAR fusion or were unaffected. At the 120 m scale, the fusion was generally more effective for  
316 single season models over multi-temporal combinations. Finally, at all scales, the annual models  
317 performed better when used together with the SAR data.



318

319

Figure 9: Model accuracies ( $R^2$  and RMSE) for Landsat-PALSAR fusion models

320

Table 3. Accuracy metrics for Landsat-PALSAR fusion models

	120 m		90 m		60 m		30 m	
	$R^2$	RMSE	$R^2$	RMSE	$R^2$	RMSE	$R^2$	RMSE
<b>Landsat Dry and Wet</b>	0.773	9.3	0.757	10	0.729	11.2	0.648	14.3
<b>Landsat Dry and Annual</b>	0.769	9.4	0.758	10	0.729	11.2	0.642	14.4
<b>Landsat Wet and Annual</b>	0.763	9.5	0.753	10.1	0.721	11.3	0.641	14.5
<b>Landsat Dry</b>	0.755	9.6	0.731	10.5	0.703	11.7	0.614	15
<b>Landsat Annual</b>	0.742	9.9	0.737	10.4	0.698	11.8	0.611	15
<b>Landsat Wet</b>	0.723	10.3	0.706	11	0.668	12.3	0.601	15.2
<b>PALSAR Only</b>	0.37	15.5	0.313	16.9	0.25	18.7	0.180	22.2

321

322

323

324

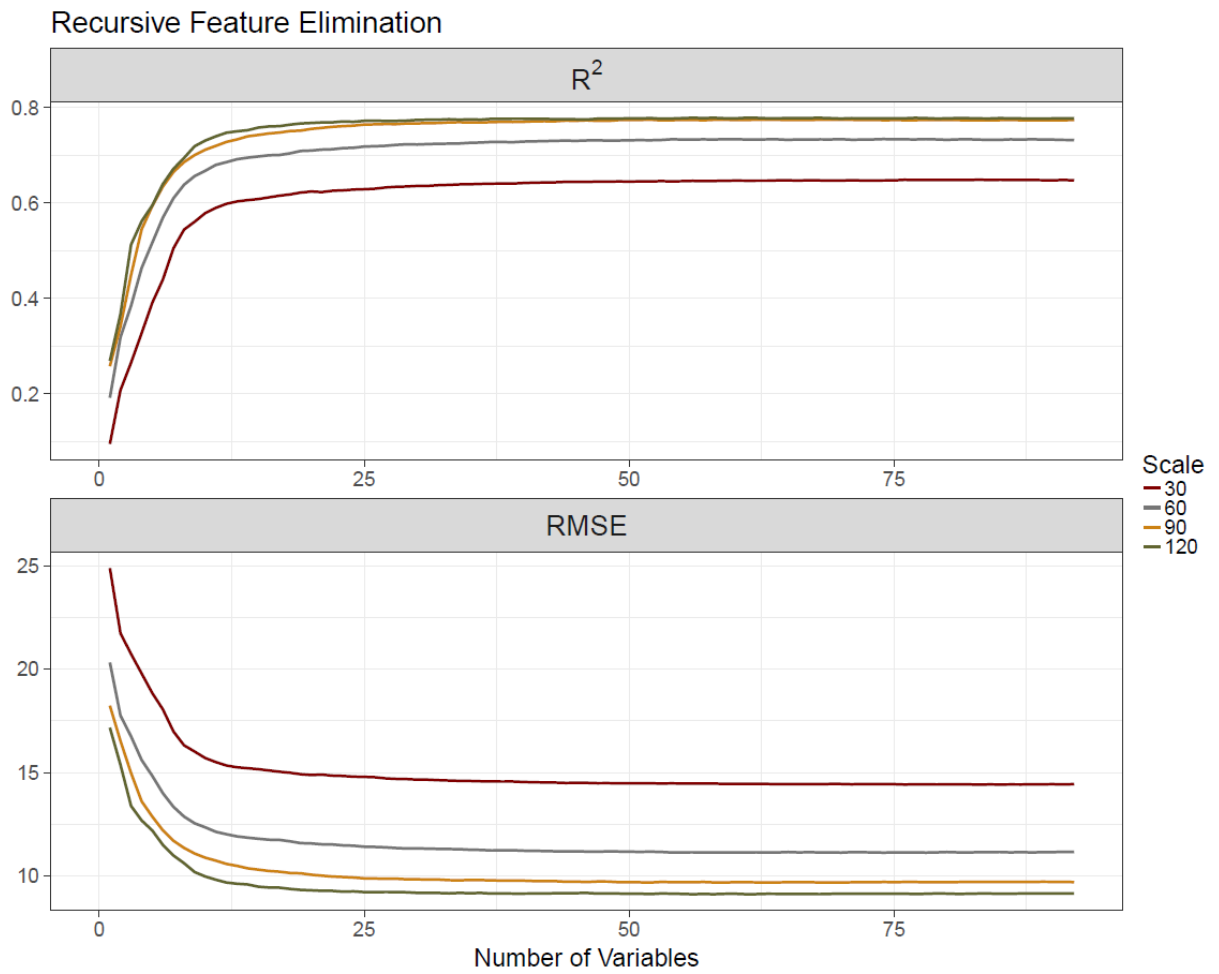
325

326 Table 4. Difference between the Landsat only and Landsat-PALSAR fusion models. Green numbers  
 327 indicate improvement from the fusion while red the opposite.

	120 m		90 m		60 m		30 m	
	R <sup>2</sup>	RMSE	R <sup>2</sup>	RMSE	R <sup>2</sup>	RMSE	R <sup>2</sup>	RMSE
<b>Landsat Dry and Wet</b>	0.003	-0.1	-0.5	0	-0.9	0.2	-0.005	0.1
<b>Landsat Dry and Annual</b>	0.006	-0.1	-0.2	0	-0.4	0.1	-0.004	0
<b>Landsat Wet and Annual</b>	0.003	-0.1	-0.3	0	-0.7	0.1	-0.002	0.1
<b>Landsat Dry</b>	0.014	-0.3	-0.1	0	-0.2	0.1	-0.004	0.1
<b>Landsat Annual</b>	0.025	-0.5	1.4	-0.3	0.9	-0.2	0.001	-0.1
<b>Landsat Wet</b>	0.009	-0.2	0.4	-0.1	-0.7	0	-0.003	0

328 **5.4 Recursive Feature Elimination (RFE)**

329 The accuracy results from the RFE automated variable selection approach is shown in Fig 10. At  
 330 all scales, model accuracies were higher when more than 25 variables were included in the model  
 331 and performance declined rapidly when fewer than that were considered. The optimal number of  
 332 variables to balance predictive accuracy and model simplicity was established as 57 for the 120 m-  
 333 pixel scale, 54 for the 90 m, 70 for the 60 m, and 85 for the 30 m, the top five variable for each model  
 334 are shown in Table 6. Applying a threshold of two standard errors, based on the cross validations  
 335 samples for the best model, allows similarly performing models to be compared (James et al., 2013).  
 336 These models ranged from the one that includes all 92 layers to a minimum of 14 variables for the  
 337 120 m scale, 20 for the 90 m scale, 29 for the 60 m, and 39 for the 30 m scale. At all scales, the model  
 338 constructed by the RFE was the best performing (Fig 11), providing an improvement in the achieved  
 339 R<sup>2</sup> of at least 0.012 (Table 5). The 120m scale RFE model was the overall most accurate (Fig 6). To  
 340 compare the within model variation in accuracy, Figure 12 shows class accuracy statistics for 10%  
 341 intervals of woody cover



342

343 Figure 10: Cross-validated R<sup>2</sup> and RMSE results from the recursive feature elimination (RFE)

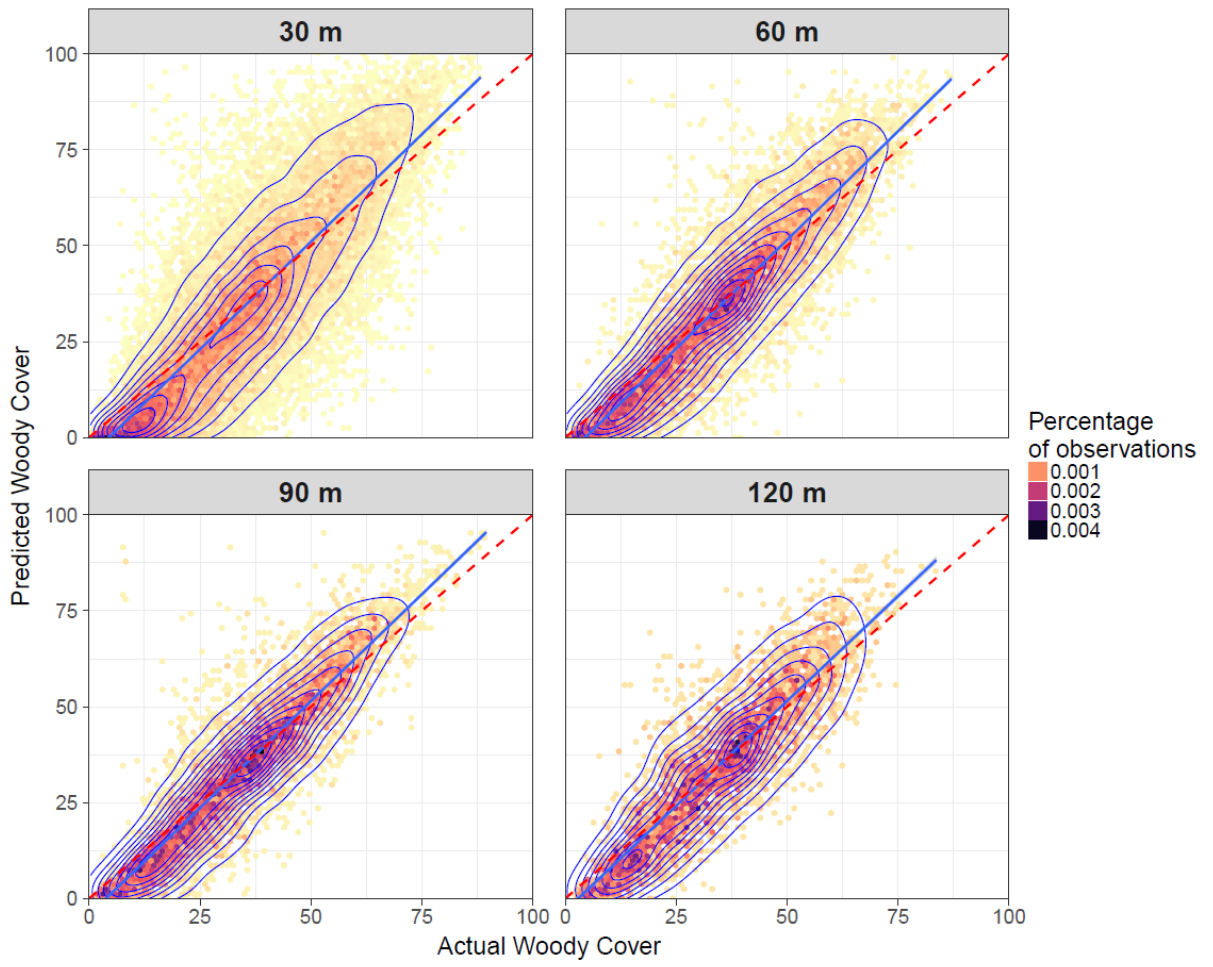
344 process

345 Table 5. Accuracy metrics for the model produced by the recursive feature elimination (RFE), all

346 92 variables, and the best Landsat-only and Landsat-SAR fused combinations.

	120 m		90 m		60 m		30 m	
	R <sup>2</sup>	RMSE	R <sup>2</sup>	RMSE	R <sup>2</sup>	RMSE	R <sup>2</sup>	RMSE
<b>Recursive Feature Elimination</b>	0.789	8.9	0.777	9.7	0.75	11.	0.661	14.2
<b>All 92 Variables</b>	0.778	9.2	0.767	9.8	0.741	11.	0.655	14.2
<b>Landsat Dry and Wet</b>	0.77	9.4	0.762	10	0.738	11.	0.653	14.2
<b>Landsat Dry and Wet + SAR</b>	0.773	9.3	0.757	10	0.729	11.2	0.648	14.3

347



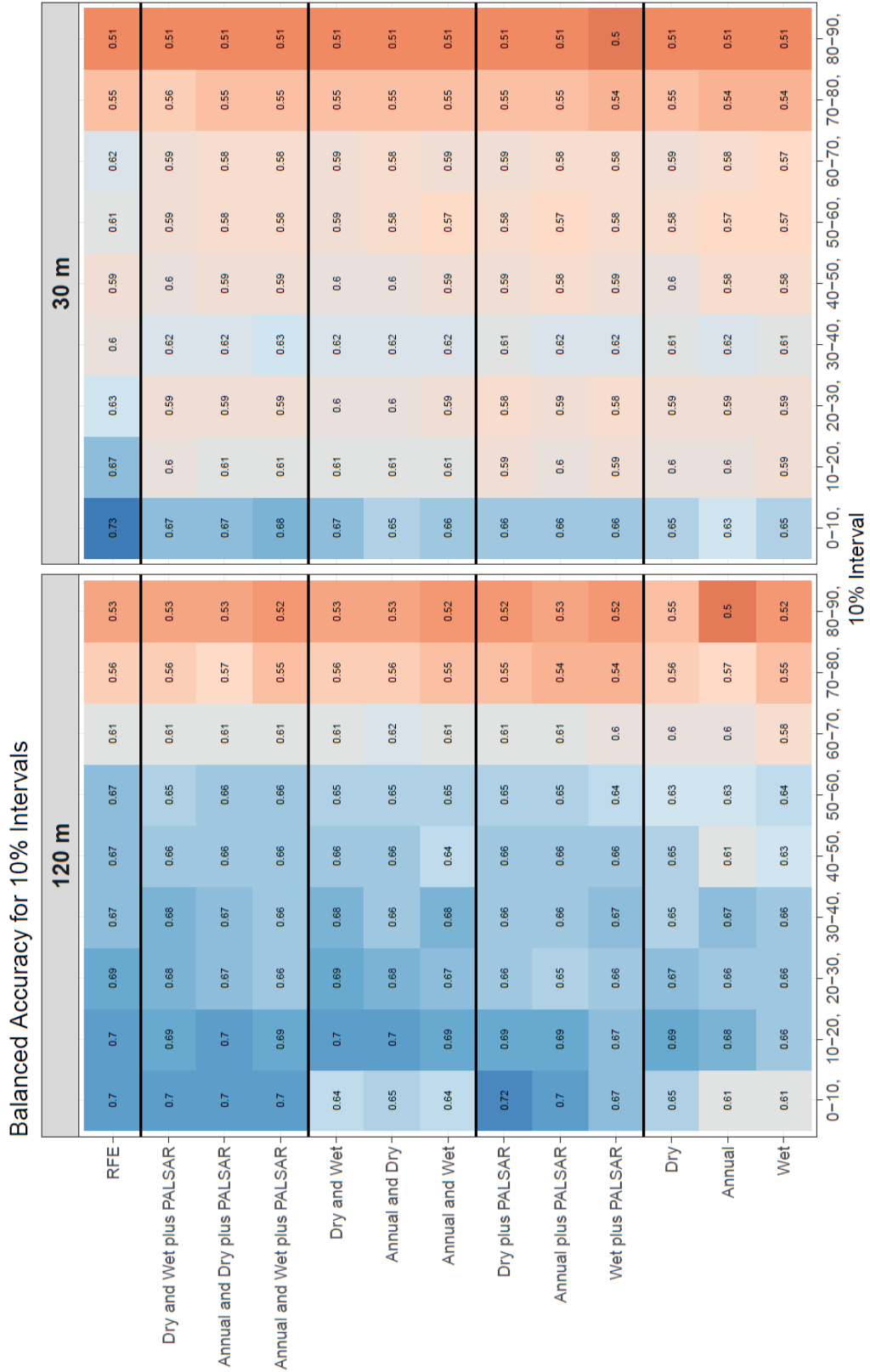
348

349

Figure 11 Density scatter plot of the Recursive Feature Elimination models at the four resolutions



350  
 351  
 352  
 353  
 354





	<b>30 m</b>	<b>60 m</b>	<b>90 m</b>	<b>120 m</b>
1	<b>HH</b>	HH	HV	HV
2	<b>B1 SD Dry</b>	B1 SD Dry	HH	HH
3	<b>B2 SD Dry</b>	B4 SD Dry	B4 Median Annual	B3 Median Annual
4	<b>B4 Median Wet</b>	HV	B3 Median Dry	B5 Median Dry
5	<b>B4 SD Dry</b>	B1 Min Wet	B3 Median Annual	B3 Median Dry

355 Table 6: Top five variables from the Recursive Feature Elimination model, at each scale (30m,  
356 60m, 90m and 120m). SD: standard deviation.

## 357 6 Discussion

### 358 6.1 Landsat metrics, seasonality and scale

359 The accuracies obtained from the Landsat-derived woody cover maps varied according to the  
360 temporal window for which metrics were calculated. For single season data, the dry period metrics  
361 were the most useful. This result was anticipated due to the persistence of green shrubs into the dry  
362 season, compared with the grass layer (Fig 2; Naidoo et al., 2016). This makes woody cover easier to  
363 discriminate, compared to other periods where differences are less pronounced (Brandt et al., 2016).  
364 This can also explain the overestimation of wet season models in Fig 7, as the grass and wood layers  
365 are more difficult to separate and identify.

366 The distribution of errors also varied with seasonality. Dry season metrics performed better in  
367 areas of sparse woody cover (0-30% cover), whereas wet metrics offered marginal improvements in  
368 the 30-40% and 50-60% percentiles (Fig 12). This can be attributed to the dry season metrics having  
369 relatively a greater discriminatory power at sparse coverage where woody canopies are more distinct.

370 Furthermore, some areas of moderate woody coverage were under-predicted by dry season only  
371 metrics. This can be attributed to the fact that some woody species are less persistent in dry  
372 conditions (Subset B in Fig 7).

373 The best result from the multi-seasonal Landsat comparisons was the combination of dry and wet  
374 season metrics. Although wet season metrics were the least effective mono-temporal models, when  
375 combined with the contrasting dry season, the information covering the peak biomass period was  
376 beneficial. This improvement was mainly limited to coverage between 10 and 70 % where each  
377 percentile produced greater class accuracies than either single-season case, at both fine (30 m) and  
378 coarse (120 m scales). In general, the multi-seasonal combinations improved prediction across the  
379 full range of woody cover densities, with the 10-40% percentiles, at 120 m resolution, achieving the  
380 highest-class accuracies. The ability to extract multiple sets of metrics from a time-series of images is  
381 noteworthy, reducing to a certain extent the drawback of a temporally limited Landsat archive in  
382 many savannah regions.

383 As fractional woody cover approaches the highest values (>70%), all models perform poorly with  
384 no model achieving a percentile class accuracy of more than 56% (Fig 12). This is partly due to the  
385 rare occurrence of this class, which affects the regression analysis. The poor accuracy for dense  
386 woody savannahs has been noted by numerous other studies (e.g. Bucini et al., 2010, Naidoo et al.,  
387 2016), and should be a priority for future studies.

388 We tested models at four scales: 30, 60, 90, and 120 m pixels. As pixel size increased, model  
389 accuracies consistently improved (Figs 8 and 9). The largest improvement occurred with the initial  
390 aggregation from 30 to 60 m, with a mean  $R^2$  increase of  $13.09\% \pm 0.9$ , across the 13 models tested.  
391 However, this change must be considered with the distribution of the input training values. At 30 m,  
392 there is a relatively larger spread of values and a higher proportion of dense and sparse woody  
393 coverage (Fig 5). Accordingly, this distribution is a more complicated endeavour for the regression  
394 analysis, as indicated by the low class accuracies for high cover percentiles (Fig 12). Concurrently, the

395 greater proportion, and pixel purity, of sparsely (0-10%) wooded areas at 30 m result in comparably  
396 high class accuracies for the first percentile class (Fig 12). Resampling to a coarser resolution reduces  
397 the occurrence of dense woody coverage, due to central tendency, making the regression exercise  
398 easier. This simplification is restricted to the 30 to 60 m aggregation with no visual or statistical  
399 evidence that additional resampling improves the outcome of the regression. Further reductions in  
400 the pixel resolution result in more modest but consistent improvements of  $4.20\% \pm 0.74$  and  
401  $1.30\% \pm 0.99$  in the  $R^2$  when re-scaling from 60 to 90 m and from 90 to 120 m, respectively. At coarser  
402 scales, artefacts from the Landsat processing are likely to be smoothed, as errors resulting from the  
403 Scan Line Corrector failure and undetected clouds are minimised (Fig 7). Furthermore, despite the  
404 high georeferencing accuracy of the datasets, errors from potential misalignment of the training  
405 imagery and Landsat data may be more prevalent at 30 m and averaged at coarser scales. For many  
406 regional-scale applications, land cover maps at 90 or 120 m may be sufficient, and an accuracy vs.  
407 precision trade-off might be appropriate. Maps at 120 m may be more accurate, but have less fidelity  
408 for detecting the clumps and canopies of dryland vegetation. This trade off may become more  
409 pertinent with the availability of 10-20 m imagery from Sentinel-2 (Bastin et al., 2017) .

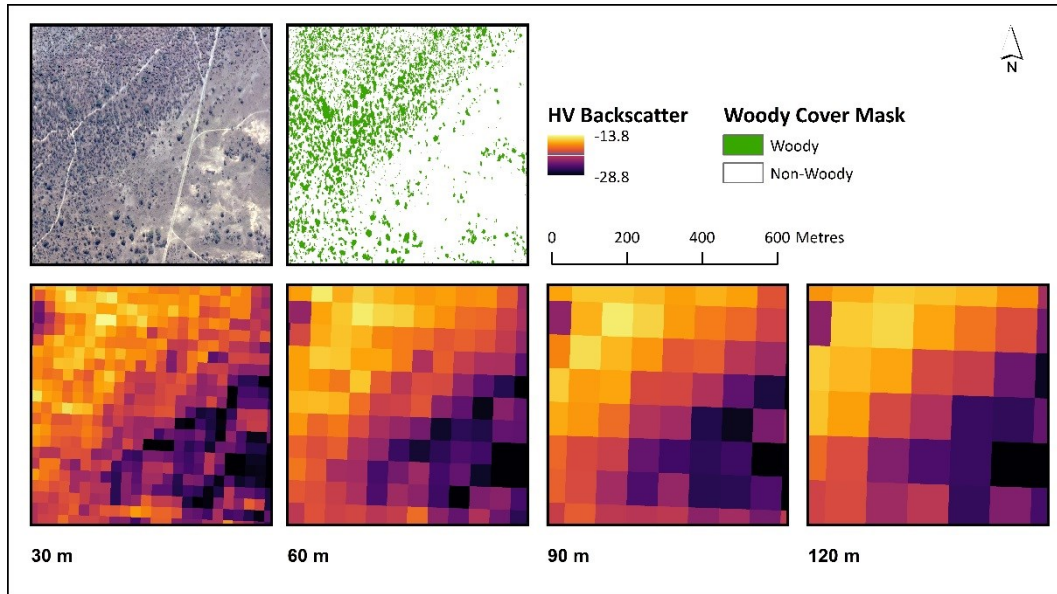
410 Overall, the accuracies achieved by the Landsat-based models are comparable to those of radar-  
411 based studies at similar scales. Urbazaev et al., (2015) achieved  $R^2$  values of 0.71 and 0.66 using  
412 multiple and single season PALSAR images at 50 m resolution, respectively, whilst Naidoo et al.,  
413 (2016) obtained  $R^2$  of 0.8 and 0.81 using single-season PALSAR data at 105 m. Given our  
414 considerably larger study area, our results are promising for regional-scale analysis, as the spatial  
415 breadth, temporal depth, and rapid processing potential of the Landsat archive is unmatched by any  
416 radar system (Kennedy et al., 2014, Roy et al., 2014). Our metrics-based approach outperforms the  
417 various single date Landsat scenarios across multiple seasons achieved by Naidoo et al. (2016) who  
418 reported  $R^2$  values of 0.32-0.65 at 105 m resolution. There are clear benefits to quantifying seasonal  
419 variability using metrics, as demonstrated by the high ranking of standard deviation layers (Table 6).  
420 Furthermore, multi-seasonal metrics further improved results over multi-seasonal image

421 combinations. We attributed this refinement to two factors: firstly, metrics are more resistant to  
422 bias incurred by rainfall and moisture variation; secondly, metrics such as standard deviation can  
423 represent the temporal profile of the land cover, imitating time-series approaches. This is in  
424 agreement with Müller et al. (2015), who found that annual metrics outperform best available pixel  
425 composites for tropical savannahs in Brazil.

426 Large-area mapping of savannah systems remains a challenge due to high heterogeneity and  
427 subjective biome classifications (Herold et al., 2008, Hüttich et al., 2011). Current approaches for  
428 regional-scale mapping generally focus on best-available pixel composites for classification (Griffiths  
429 et al., 2013, White et al., 2014, Frantz et al., 2017). Due to the high temporal variation in savannahs,  
430 this method is particularly vulnerable to bias effects caused by pixels being selected in different  
431 phenological stages (Hüttich et al., 2011, Müller et al., 2015). We demonstrate that Landsat-based  
432 spectral variability metrics offer a robust alternative for land cover mapping at large spatial scales,  
433 applicable to epochal or annual analyses. South Africa possesses good availability of Landsat imagery  
434 in the USGS archive, owing to the successful transfer of data from the Johannesburg receiving station,  
435 active since 1980 (Wulder et al., 2015). However, in many savannah regions, such as the Sahel and  
436 east Africa, the historical Landsat archive is sparse. By combining multiple years of observations, wall-  
437 to-wall mapping should be possible even with low annual image availability. Furthermore,  
438 segmenting a time-series into multiple temporal windows allows additional value to be extracted  
439 from a single series of observations, potentially compensating for a relatively limited archive. The  
440 high image acquisition rate of Landsat 8 relative to the historic Landsat archive, combined with  
441 comparable imagery from the Sentinel-2 satellites, will result in improved temporal resolution for  
442 optical imagery (Drusch et al., 2012, Roy et al., 2014). Increased observations should enable our multi-  
443 seasonal metrics approach to be expanded by using more or smaller temporal windows, for example  
444 the beginning or ending of the dry season. Evidence from MODIS-based studies suggests that this  
445 refinement may allow increased discrimination of subtle land covers, such as densely wooded  
446 savannahs, which are currently poorly mapped (Hüttich et al., 2009).

## 447 6.2 Landsat-PALSAR fusion

448 Integrating the Landsat metrics with L-band PALSAR backscatter had divergent impacts. Finer-  
449 scale maps (30 to 90 m) were negatively affected by the inclusion of radar, with the Landsat-only  
450 models outperforming their fused counterparts (Table 4). Comparably, the PALSAR-only models  
451 performed poorly, especially at fine-scales (Table 3). We attribute this to the high-level of noise in  
452 radar imagery at higher resolutions, as illustrated in Fig 13. Errors caused by factors such as speckle,  
453 moisture content and geolocation accuracy are far more prevalent in finer-scale radar data.  
454 Therefore, at 30 to 90 m pixel scales, the PALSAR imagery contains a weak signal-to-noise ratio,  
455 incurring a negative impact on the regression model. This is further reflected in the increasing ranks  
456 of radar variables in the Recursive Feature Elimination (RFE, Table 6). Accordingly, SAR-fusion reduced  
457 class accuracy by ~1% for area 20-60% coverage, at 30 m scales (Fig 12). Conversely, the coarse scale  
458 models (120 m) were consistently improved by the addition of PALSAR backscatter to the Landsat  
459 metrics, with the single-season combinations undergoing the greatest improvement. The lower  
460 improvements for the multi-seasonal scenarios indicates that some of the information contained in  
461 radar backscatter can be obtained from multi-seasonal metrics. The inclusion of L-band radar had the  
462 highest impact on sparse woody cover classes (0-30%). Within these classes, inclusion of the SAR  
463 variables increased balanced accuracies by 1-9% and 1-2%, at 120 and 30 m scales, respectively (Fig  
464 12). Visual examination of the prediction subset maps indicates that this improvement is due to the  
465 SAR fusion correcting for overestimations when there is 0 - 20 % woody cover (e.g. the central pivot  
466 irrigation fields in Subset A of Fig 7).



467

468 Figure 13: Subsets of HV polarized PALSAR backscatter across a grassland-shrub transition at  
 469 different resolutions

470 Multi-sensor fusion approaches are becoming more popular, due to an increase in the number of  
 471 operational sensors and the open-access data policies. The improvements at coarse scales are in line  
 472 with those found in other studies employing SAR and Landsat data together (Bucini et al., 2010,  
 473 Naidoo et al., 2016). However, this study is the first to quantify the effect and mechanism of this  
 474 fusion across multiple seasons and scales. The accuracies of the PALSAR-only models generated here  
 475 are lower than other South African studies (e.g. Naidoo et al., 2016, Urbazaev et al., 2015). We  
 476 attribute this to the much larger and heterogeneous study area that we cover, encompassing human  
 477 modified landscapes where the other two studies were confined within the Kruger National Park. The  
 478 source of training data could also have affected the accuracy of our PALSAR-based estimates: we  
 479 employ aerial photographs while Naidoo et al. (2016) and Urbazaev et al. (2015) use more accurate  
 480 characterisations from the field or from LiDAR sources. It should also be noted that our study used a  
 481 mosaicked ALOS PALSAR layer produced from images acquired across a three month window (1<sup>st</sup> July  
 482 - 3<sup>rd</sup> October), including two images acquired in the previous year. Seasonal effects, such as canopy  
 483 density and moisture content, may prevent the mosaicked images from being artefact-free.  
 484 Alternatively, the global-scale processing undertaken in the creation of the mosaicked PALSAR layer,

485 such as speckle reduction and topographic normalisation, may reduce the fidelity of backscatter  
486 measurements when compared to scene-specific methods applied elsewhere (e.g. Naidoo et al.,  
487 2016, Urbazaev et al., 2015). Furthermore, multi-sensor fusion has a potential for image miss-  
488 registration errors between the imagery (Lehmann et al., 2015).

489 Although overall model accuracies are only moderately changed by the inclusion of L-band SAR  
490 data, the consistent allocation of improvements at low densities of woody cover may be highly  
491 relevant to semi-arid savannah case studies. The process of shrub encroachment into grasslands is a  
492 major threat to the livelihoods of many pastoralists in the developing world. For prevention and  
493 remediation to be successful, action must be taken as early as possible. The periodic monitoring of  
494 sparsely wooded savannahs, which are vulnerable to shrub encroachment, is therefore a pressing  
495 requirement. For this purpose, the fusion of PALSAR and Landsat imagery is beneficial, offering a  
496 higher likelihood of timely change detection than single-sensor approaches. In the coming years,  
497 fusion techniques based C-band radar from Sentinel-1 may offer good promise, owing to the 12 day  
498 revisit time.

### 499 6.3 Merit of variable reduction methods

500 To ascertain the value of variable reduction methods we applied a Recursive Feature Elimination  
501 (RFE) on out 92 variable dataset. The RFE produced the best performing model at all scales, compared  
502 to all Landsat and Landsat-PALSAR fusion cases (Fig 11). In general, the number of variables used in  
503 the RFE models decreased with aggregation: we attribute the requirement of less variables at coarser  
504 resolutions to improvements in signal-to-noise ratios as noisier layers are smoothed. Dimension  
505 reduction methods are also useful for highlighting the type of variables that contain useful  
506 information for the model building. The high ranking of standard deviation - a proxy for seasonal  
507 variability highlights the importance of temporal information for woody cover mapping.

508 As both the number of active sensors and the availability of open data archives increase, remote  
509 sensing analyses are using high-dimensional datasets. The utility of variable selection or dimension  
510 reduction methods will inevitably increase in order to deal with the increasing data volume. Currently,  
511 these tools are primarily used in hyperspectral analyses, but are underutilised in other areas (Pal and  
512 Foody 2010). The fact that the RFE was able to automate the process of selecting a superior model  
513 highlights the potential of automating model construction using machine learning methods that may  
514 currently be underused (Meyer et al., 2016). At large-scales, mapping land cover with fewer variables  
515 can drastically reduce processing time, leaving unnecessary variables out can therefore be useful for  
516 computing and statistical purposes.

## 517 7 Conclusions

518 We tested the potential of Landsat-derived spectral variability metrics and PALSAR composites  
519 for mapping woody coverage, in southern African savannas. We compared the role of seasonal  
520 compositing period, and the effect of multi-sensor fusion through the addition of ALOS PALSAR  
521 backscatter to the Landsat layers. Furthermore, we investigated the role of pixel scale on map  
522 accuracy, and the potential of variable selection methods for automating the model building  
523 process.

524 We draw a number of conclusions from our modelling scenarios. Firstly, Landsat metrics can  
525 produce highly accurate maps of fractional cover in savannas, with dry season imagery being the  
526 preferred temporal window. Further improvements can be made by combining multi-seasonal  
527 metrics, derived from two contrasting seasons. In particular, integrating dry and wet season layers  
528 produced good improvements in map accuracy. Secondly, the fusion of Landsat and PALSAR layers  
529 is not always beneficial. At fine scales (30-60 m), L-band SAR integration reduced model  
530 performance consistently, potentially due to the high level of noise inherent to radar data,



531 particularly in savannahs. Conversely, at the 120 m scale, the addition of PALSAR was beneficial,  
532 particularly for areas with less than 30% coverage, and for some models at 90 m scales as well.  
533 Finally, the use of a recursive feature elimination automated variable selection process was very  
534 efficient in constructing an accurate parsimonious model, producing the most effective model at  
535 every scale examined whilst reducing the number of variables used to of 57 out of 90.

536 In summary, Landsat metrics offer a suitable option for regional-scale mapping of savannah  
537 woody cover, and should allow decadal scale analysis of land cover changes. The use of multi-  
538 seasonal composites are particularly promising for accurate fractional woody cover mapping. For  
539 contemporary monitoring, the fusion of Landsat metrics with L-band radar is recommended for  
540 areas with lower woody cover densities, and particularly for the rapid detection of shrub  
541 encroachment into grass-dominated savannahs. Future studies will benefit from automated variable  
542 reduction approaches and the increased image acquisition rates from the Sentinel constellation,  
543 that feature both radar (C-Band) and optical satellites.

## 544 Acknowledgements

545 TH is funded by a Manchester Metropolitan University (MMU) Research Fellowship. ES is supported  
546 by an EU FP7 Marie Curie Career Integration Grant (PCIG12-GA-2012-3374327). We are grateful to  
547 the USGS, JAXA, and the NGI for providing the data used in this study. The authors declare no  
548 personal or financial conflicts of interest.

549

## 550 References

551 Armston, J. D., R. J. Denham, Danaher, T. J. Scarth, P. F. Mo et, and N Trevor (2009). Prediction  
552 and validation of foliage projective cover from Landsat-5 TM and Landsat-7 ETM+ imagery.  
553 Journal of Applied Remote Sensing 3.(033540).

554 Bastin, J.F., Berrahmouni, N., Grainger, A., Maniatis, D., Mollicone, D., Moore, R., Patriarca, C.,  
555 Picard, N., Sparrow, B., Abraham, E.M. and Aloui, K., 2017. The extent of forest in dryland  
556 biomes. *Science*, 356(6338), pp.635-638.

557 Brandt, M., P. Hiernaux, T. Tagesson, A. Verger, K. Rasmussen, A. A. Diouf, C. Mbow, E. Mougin,  
558 and R. Fensholt (2016). Woody plant cover estimation in drylands from Earth Observation based  
559 seasonal metrics. *Remote Sensing of Environment* 172, 28 38.

560 Breiman, L. (2001). Random forests. *Machine learning* 45.(1), 5 32.

561 Bucini, G, N. Hanan, R. Boone, I. Smit, S Saatchi, M. Lefsky, and G. Asner (2010). Woody  
562 fractional cover in Kruger National Park, South Africa: remote-sensing-based maps and  
563 ecological insights. *Ecosystem function in savannas: measurement and modelling at landscape  
564 to global scales*. Ed. by M. J. Hill and N. P. Hanan. Boca Raton, Florida: CRC Press. Chap. 11, pp.  
565 219 238.

566 Brandt, M., Rasmussen, K., Peñuelas, J., Tian, F., Schurgers, G., Verger, A., Mertz, O., Palmer, J.R.  
567 and Fensholt, R., 2017. Human population growth offsets climate-driven increase in woody  
568 vegetation in sub-Saharan Africa. *Nature Ecology & Evolution*, 1(4), pp.s41559-017.

569 Carlson, T. N. and D. A. Ripley (1997). On the relation between NDVI, fractional vegetation  
570 cover, and leaf area index. *Remote sensing of Environment* 62.(3), 241 252.

571 Drusch, M, U Del Bello, S Carlier, O Colin, V Fernandez, F Gascon, B Hoersch, C Isola, P Laberinti,  
572 P Martimort, et al., (2012). Sentinel-2: ESA's optical high-resolution mission for GMES  
573 operational services. *Remote Sensing of Environment* 120, 25 36.

574 Frantz, D., Röder, A., Stellmes, M. and Hill, J. (2017) Phenology-adaptive pixel-based  
575 compositing using optical earth observation imagery. *Remote Sensing of Environment* 190. 331-  
576 347.

577 Guyon, I. and Elisseeff, A., 2003. An introduction to variable and feature selection. *Journal of  
578 machine learning research*, 3.1157-1182.

579 Griffiths, P., S. Van Der Linden, T. Kuemmerle, and P. Hostert (2013). A pixel-based Landsat  
580 compositing algorithm for large area land cover mapping. *IEEE Journal of Selected Topics in  
581 Applied Earth Observations and Remote Sensing* 6.(5), 2088 2101.

582 Guerschman, J.P., Hill, M.J., Renzullo, L.J., Barrett, D.J., Marks, A.S. and Botha, E.J., (2009).  
583 Estimating fractional cover of photosynthetic vegetation, non-photosynthetic vegetation and  
584 bare soil in the Australian tropical savanna region upscaling the EO-1 Hyperion and MODIS  
585 sensors. *Remote Sensing of Environment*, 113(5),928-945.

586 Guyon, I., J. Weston, S. Barnhill, and V. Vapnik (2002). Gene selection for cancer classification  
587 using support vector machines. *Machine learning* 46.(1-3), 389 422.

588 Herold, M, P Mayaux, C. Woodcock, A Baccini, and C Schmullius (2008). Some challenges in  
589 global land cover mapping: An assessment of agreement and accuracy in existing 1 km datasets.  
590 *Remote Sensing of Environment* 112.(5), 2538 2556.

591 Higginbottom, T. P. and E. Symeonakis (2014). Assessing Land Degradation and Desertification  
592 Using Vegetation Index Data: Current Frameworks and Future Directions. *Remote Sensing*  
593 6.(10), 9552 9575.

594 Hijmans, R. J., J. van Etten, M. Mattiuzzi, M. Sumner, J. A. Greenberg, O. P. Lamigueiro, A.  
595 Bevan, E. B. Racine, A. Shortridge, and M. R. J. Hijmans (2015). raster: Geographic Data Analysis  
596 and Modelling. R package version 2.3-40.

597 Hostert, P., Griffiths, P., van der Linden, S. and Pflugmacher, D., 2015. Time series analyses in a  
598 new era of optical satellite data. In *Remote Sensing Time Series* (pp. 25-41). Springer  
599 International Publishing.

600 Huttich, C., U. Gessner, M. Herold, B. J. Strohbach, M. Schmidt, M. Keil, and S. Dech (2009). On  
601 the suitability of MODIS time series metrics to map vegetation types in dry savanna ecosystems:  
602 A case study in the Kalahari of NE Namibia. *Remote Sensing* 1.(4), 620 643.

603 Huttich, C., M. Herold, M. Wegmann, A. Cord, B. Strohbach, C. Schmullius, and S. Dech (2011).  
604 Assessing effects of temporal compositing and varying observation periods for large-area  
605 landcover mapping in semi-arid ecosystems: Implications for global monitoring. *Remote Sensing*  
606 of Environment 115.(10), 2445 2459.

607 Gorelick, N., Hancher, M., Dixon, M., Ilyushchenko, S., Thau, D. and Moore, R., 2017. Google  
608 Earth Engine: Planetary-scale geospatial analysis for everyone. *Remote Sensing of Environment*.

609 James, G., D. Witten, T. Hastie, and R. Tibshirani (2013). An introduction to statistical learning.  
610 Springer.

611 Joseph, J and Devadas, (2015) Detection of rooftop regions in rural areas using Support Vector  
612 Machine. *International Journal of Science Research Engineering* 4 549–553

613 Kennedy, R.E., Andréfouët, S., Cohen, W.B., Gómez, C., Griffiths, P., Hais, M., Healey, S.P.,  
614 Helmer, E.H., Hostert, P., Lyons, M.B. and Meigs, G.W., Pflugmacher, D., Phinn, S.R., Powell, S.L.,  
615 Scarth, P., Sen, S., Schroeder, T.A., Schneider, A., Sonnenschein, R., Vogelmann, J.E., Wulder,  
616 M.A., Zhu, Z. (2014). Bringing an ecological view of change to Landsat based remote sensing.  
617 *Frontiers in Ecology and the Environment* 12.(6), 339 346.

618 Kottek, M., J. Grieser, C. Beck, B. Rudolf, and F. Rubel (2006). World map of the Koppen-Geiger  
619 climate classification updated. *Meteorologische Zeitschrift* 15.(3), 259 263.

620 Kuhn, M. (2015). caret: Classification and Regression Training. R package version 6.0-52.

621 Kuhn, M. and K. Johnson (2013). Applied predictive modelling. Springer.

622 Leutner, B. and N. Horning (2016). RStoolbox: Tools for Remote Sensing Data Analysis. R  
623 package version 0.1.4.

624 Lehmann EA, Caccetta P, Lowell K, Mitchell A, Zhou ZS, Held A, Milne T, Tapley I (2015). SAR and  
625 optical remote sensing: Assessment of complementarity and interoperability in the context of a  
626 large-scale operational forest monitoring system. *Remote Sensing of Environment* (156). 335-  
627 348.

628 Liaw, A. and M. Wiener (2002). Classification and regression by randomForest. *R news* 2.(3), 18  
629 22.

630 Lucas, R. M., N. Cronin, M. Moghaddam, A. Lee, J. Armston, P. Bunting, and C. Witte (2006).  
631 Integration of radar and Landsat-derived foliage projected cover for woody regrowth mapping,  
632 Queensland, Australia. *Remote Sensing of Environment* 100.(3), 388 406.

633 Ludwig, A, H Meyer, and T Nauss (2016). Automatic classification of Google Earth images for a  
634 larger scale monitoring of bush encroachment in South Africa. *International Journal of Applied*  
635 *Earth Observation and Geoinformation*.

636 Main, R., R. Mathieu, W. Kleynhans, K. Wessels, L. Naidoo, and G. P. Asner (2016). Hyper-  
637 temporal C-band SAR for baseline woody structural assessments in deciduous savannas.  
638 *Remote Sensing* 8.(8), 661.

639 Mathieu, R. et al., (2013). Toward structural assessment of semi-arid African savannahs and  
640 woodlands: The potential of multitemporal polarimetric RADARSAT-2 beam images. *Remote*  
641 *Sensing of Environment* 138, 215 231.

642 Meyer, H., M. Katurji, T. Appelhans, M. U. Muller, T. Nauss, P. Roudier, and P. Zawar-Reza  
643 (2016). Mapping Daily Air Temperature for Antarctica Based on MODIS LST. *Remote Sensing*  
644 8.(9), 732.

645 Mitchard, E., S. Saatchi, I. Woodhouse, G Nangendo, N. Ribeiro, M Williams, C. Ryan, S. Lewis, T.  
646 Feldpausch, and P Meir (2009). Using satellite radar backscatter to predict aboveground woody  
647 biomass: A consistent relationship across four different African landscapes. *Geophysical*  
648 *Research Letters* 36.(23).

649 Moore, R.T. and Hansen, M.C., (2011) Google Earth Engine: a new cloud-computing platform for  
650 global-scale earth observation data and analysis. AGU Fall Meeting Abstracts..

651 Mucina, L and M. Rutherford, eds. (2006). *The vegetation of South Africa, Lesotho and*  
652 *Swaziland*. Pretoria: South African National Biodiversity Institute.

653 Muller, H., P. Ru n, P. Griffiths, A. J. B. Siqueira, and P. Hostert (2015). Mining dense Landsat time  
654 series for separating cropland and pasture in a heterogeneous Brazilian savanna landscape.  
655 *Remote Sensing of Environment* 156, 490 499.

656 Naidoo, L., R. Mathieu, R. Main, W. Kleynhans, K. Wessels, G. Asner, and B. Leblon (2015).  
657 Savannah woody structure modelling and mapping using multi-frequency (X-, C-and L-band)  
658 Synthetic Aperture Radar data. *ISPRS Journal of Photogrammetry and Remote Sensing* 105, 234  
659 250.

660 Naidoo, L., R. Mathieu, R. Main, K. Wessels, and G. P. Asner (2016). L-band Synthetic Aperture  
661 Radar imagery performs better than optical datasets at retrieving woody fractional cover in  
662 deciduous, dry savannahs. *International Journal of Applied Earth Observation and*  
663 *Geoinformation* 52, 54 64.

664 Naito, A. T. and D. M. Cairns (2011). Patterns and processes of global shrub expansion. *Progress*  
665 *in Physical Geography* 35.(4), 423 442.

666 National Geo-spatial Information (2017) Colour Digital Aerial Imagery [online].  
667 [http://www.ngi.gov.za/index.php/what-we-do/aerial-photography-and-imagery/35-colour-](http://www.ngi.gov.za/index.php/what-we-do/aerial-photography-and-imagery/35-colour-digital-aerial-imagery-at-0-5m-gsd-2008-2016-and-0-25m-gsd-2017-current)  
668 [digital-aerial-imagery-at-0-5m-gsd-2008-2016-and-0-25m-gsd-2017-current](http://www.ngi.gov.za/index.php/what-we-do/aerial-photography-and-imagery/35-colour-digital-aerial-imagery-at-0-5m-gsd-2008-2016-and-0-25m-gsd-2017-current)

669 Olsson, A. D., W. J. van Leeuwen, and S. E. Marsh (2011). Feasibility of invasive grass detection  
670 in a desertscrub community using hyperspectral field measurements and Landsat TM imagery.  
671 *Remote Sensing* 3.(10), 2283 2304.

672 Pal, M. and G. M. Foody (2010). Feature selection for classification of hyperspectral data by  
673 SVM. *IEEE Transactions on Geoscience and Remote Sensing* 48.(5), 2297 2307.

674 Prince, S.D. and Astle, W.L., 1986. Satellite remote sensing of rangelands in Botswana I. Landsat  
675 MSS and herbaceous vegetation. *International Journal of Remote Sensing*, 7(11) .1533-1553.

676 Pollard, S., C. Shackleton, and J. Carruthers (2003). Beyond the fence: people and the lowveld  
677 landscape. *The Kruger experience: Ecology and management of savanna heterogeneity*. Ed. by J.  
678 T. Du Toit, K. H. Rogers, and H. C. Biggs. Washington: Island Press. Chap. 7, pp. 422-446.

679 R Core Team (2015). *R: A Language and Environment for Statistical Computing*. R Foundation for  
680 Statistical Computing. Vienna, Austria.

681 Reiche, J., Lucas, R., Mitchell, A.L., Verbesselt, J., Hoekman, D.H., Haarpaintner, J., Kellendorfer,  
682 J.M., Rosenqvist, A., Lehmann, E.A., Woodcock, C.E. and Seifert, F.M., 2016. Combining satellite  
683 data for better tropical forest monitoring. *Nature Climate Change*, 6(2), p.120.

684 Rosenqvist, A., M. Shimada, N. Ito, and M. Watanabe (2007). ALOS PALSAR: A pathfinder  
685 mission for global-scale monitoring of the environment. *IEEE Transactions on Geoscience and  
686 Remote Sensing* 45.(11), 3307-3316.

687 Roy, D. P., M. Wulder, T. Loveland, C. Woodcock, R. Allen, M. Anderson, D. Helder, J. Irons, D.  
688 Johnson, R. Kennedy, et al., (2014). Landsat-8: Science and product vision for terrestrial global  
689 change research. *Remote Sensing of Environment* 145, 154-172.

690 Sankaran, M., N. P. Hanan, R. J. Scholes, J. Ratnam, D. J. Augustine, B. S. Cade, J. Gignoux, S. I.  
691 Higgins, X. Le Roux, and F. Ludwig (2005). Determinants of woody cover in African savannas.  
692 *Nature* 438.(7069), 846-849.

693 Scholes, R., N. Gureja, M. Giannecchini, D. Dovie, B. Wilson, N. Davidson, K. Piggott, C. McLoughlin,  
694 K. Van der Velde, A. Freeman, et al., (2001). The environment and vegetation of the flux  
695 measurement site near Skukuza, Kruger National Park. *Koedoe* 44.(1), 73-83.

696 Shimada, M. and T. Ohtaki (2010). Generating large-scale high-quality SAR mosaic datasets:  
697 Application to PALSAR data for global monitoring. *IEEE Journal of Selected Topics in Applied  
698 Earth Observations and Remote Sensing* 3.(4), 637-656.

699 Shimada, M., T. Itoh, T. Motooka, M. Watanabe, T. Shiraishi, R. Thapa, and R. Lucas (2014). New  
700 global forest/non-forest maps from ALOS PALSAR data (2007-2010). *Remote Sensing of  
701 Environment* 155, 13-31.

702 Staben, G.W., Lucieer, A., Evans, K.G., Scarth, P. and Cook, G.D., 2016. Obtaining biophysical  
703 measurements of woody vegetation from high resolution digital aerial photography in tropical  
704 and arid environments: Northern Territory, Australia. *International Journal of Applied Earth  
705 Observation and Geoinformation*, 52, pp.204-220.

706 Skowno, A.L., Thompson, M.W., Hiestermann, J., Ripley, B., West, A.G. and Bond, W.J., 2017.  
707 Woodland expansion in South African grassy biomes based on satellite observations (1990–  
708 2013): general patterns and potential drivers. *Global change biology*, 23(6), pp.2358-2369.

709 Stevens, N., Lehmann, C.E., Murphy, B.P. and Durigan, G., 2017. Savanna woody encroachment  
710 is widespread across three continents. *Global change biology*, 23(1), pp.235-244.

711 Tian, F., Brandt, M., Liu, Y.Y., Rasmussen, K. and Fensholt, R., 2017. Mapping gains and losses in  
712 woody vegetation across global tropical drylands. *Global change biology*, 23(4), pp.1748-1760.

713 Urbazaev, M., C. Thiel, R. Mathieu, L. Naidoo, S. R. Levick, I. P. Smit, G. P. Asner, and C.  
714 Schullius (2015). Assessment of the mapping of fractional woody cover in southern African  
715 savannas using multi-temporal and polarimetric ALOS PALSAR L-band images. *Remote Sensing*  
716 *of Environment* 166, 138-153.

717 Wessels, K. J., M. S. Colgan, B. F. N. Erasmus, G. P. Asner, W. C. Twine, R. Mathieu, J. A. N. Van  
718 Aardt, J. T. Fisher, and I. P. J. Smit (2013). Unsustainable fuelwood extraction from South African  
719 savannas. *Environmental Research Letters* 8.(1).

720 Worden, N., (1994). *The making of modern South Africa: conquest, segregation, and apartheid.*  
721 Juta and Company Ltd.

722 White, J., M. Wulder, G. Hobart, J. Luther, T. Hermosilla, P. Griffiths, N. Coops, R. Hall, P. Hostert,  
723 A. Dyk, et al., (2014). Pixel-based image compositing for large-area dense time series  
724 applications and science. *Canadian Journal of Remote Sensing* 40.(3), 192-212.

725 Wulder, M. A., J. C. White, T. R. Loveland, C. E. Woodcock, A. S. Belward, W. B. Cohen, E. A.  
726 Fosnight, J. Shaw, J. G. Masek, and D. P. Roy (2015). The global Landsat archive: Status,  
727 consolidation, and direction. *Remote Sensing of Environment* 185, 271-283.

728 Zhong, L., P. Gong, and G. S. Biging (2014). Efficient corn and soybean mapping with temporal  
729 extendibility: A multi-year experiment using Landsat imagery. *Remote Sensing of Environment*  
730 140, 1-13.

731 Zhu, Z., J. Bi, Y. Pan, S. Ganguly, A. Anav, L. Xu, A. Samanta, S. Piao, R. R. Nemani, and R. B.  
732 Myneni (2013). Global data sets of vegetation leaf area index (LAI) 3g and Fraction of  
733 photosynthetically Active Radiation (FPAR) 3g derived from Global Inventory Modelling and  
734 Mapping Studies (GIMMS) Normalized Difference Vegetation Index (NDVI3g) for the period  
735 1981 to 2011. *Remote Sensing* 5.(2), 927-948.

736 Zhu, Z. and Woodcock, C.E., (2012). Object-based cloud and cloud shadow detection in Landsat  
737 imagery. *Remote Sensing of Environment*, 118, 83-94.

738  
739  
740  
741  
742  
743  
744  
745

## 746 Appendix

747 Table A1 Woody cover mask classification accuracies.

Mask Number	Date	Accuracy	Sensitivity	Specificity
-------------	------	----------	-------------	-------------

<b>1</b>	19/04/2009	0.74	0.73	0.75
<b>2</b>	30/04/2009	0.85	0.88	0.80
<b>3</b>	01/05/2009	0.85	0.88	0.80
<b>4</b>	07/08/2008	0.87	0.87	0.88
<b>5</b>	23/06/2008	0.85	0.86	0.85
<b>6</b>	01/06/2008	0.92	0.88	0.95
<b>Positive Class: Woody Cover</b>				

748

749